https://doi.org/10.5194/egusphere-2026-4085
Preprint. Discussion started: 4 August 2026

Atmospheric Tidal Variability and Gravity Wave Forcing During the January 19-21, 2026 Geomagnetic Storm

Tesfau Hagos Tadesse[a,*], Gebregiorgis Abraha Fikade[a], Yikdem Mengesha Gebrehiwot[a], Tesfay Lijalem Weldeslasie[a]

[a] *Department of Physics, Mekelle University, tesfulidya25@gmail.com, ggabraha@gmail.com, yikdema16@gmail.com, tesabrsh@gmail.com, Mekelle, Tigray, Ethiopia*

Abstract

This study investigates the variability of migrating atmospheric tides and gravity wave forcing in the mesosphere and lower thermosphere (MLT) during the geomagnetic storm of January 19-21, 2026. Using GNSS, Swarm and SABER observations to compare quiet (January 16–18 and January 28-30) and disturbed January 19-21, 2026 conditions respectively, we study the evolution of diurnal, semidiurnal, terdiurnal, and quarterdiurnal tidal components alongside gravity wave activity and thermal structure variations. Results reveal a 21% storm-time amplification of semidiurnal and terdiurnal tides, accompanied by phase shifts at 20^o North, 20^o South and the emergence of non-migrating tidal components. Gravity waves exhibit enhanced amplitudes by 43%, increased intermittency, and reduced vertical coherence, indicating strong wave mean flow interactions and localized dissipation. These findings demonstrate a tightly coupled system in which geomagnetic forcing modifies the background thermospheric winds and temperature structures, thereby altering tidal propagation pathways and filtering gravity wave dynamics. This study provides quantified evidence of the importance of multi-scale vertical and latitudinal interactions during intense geomagnetic disturbances.

Keywords: Atmospheric tides; Gravity waves; Geomagnetic storm; Thermosphere; Wave coupling; Tidal variability

*Corresponding author: Tesfau Hagos Tadesse
Email: tesfulidya25@gmail.com

https://doi.org/10.5194/egusphere-2026-4085
Preprint. Discussion started: 4 August 2026

1. Introduction

Atmospheric tides and gravity waves are fundamental drivers of vertical coupling in the Earth's atmosphere. Migrating tides, primarily generated by solar heating, exhibit periodic structures, such as diurnal (24 h), semidiurnal (12 h), terdiurnal (8 h), and quarterdiurnal (6 h) oscillations. Gravity waves, on the other hand, originate mainly in the lower atmosphere and propagate upward, transferring momentum and energy(Bretherton, 1969). During geomagnetic storms, enhanced solar wind–magnetosphere interaction leads to significant perturbations in the thermosphere–ionosphere system(Rees, 1995). Energy inputs such as Joule heating and particle precipitation modify temperature, density, and wind structures, thereby affecting tidal propagation and gravity wave dynamics(Ravinuthala et al., 2022).

The upper atmosphere, particularly the mesosphere and thermosphere, is a highly dynamic region where energy and momentum are continuously exchanged between lower atmospheric processes and space weather drivers(Killeen and Johnson, 1995). Among the key mechanisms controlling this region are atmospheric tides and gravity waves, which play a fundamental role in regulating global circulation, thermospheric structure, and ionospheric variability(Ortland and Alexander, 2006). Atmospheric tides, primarily driven by solar heating and latent heat release, provide large-scale periodic variability, while gravity waves generated from lower atmospheric sources contribute to small-scale perturbations and vertical coupling (Forbes et al., 2020); (Hagan and Forbes, 2002); (Chapman and Lindzen, 1969). The interaction between these two dynamical systems is essential for understanding the variability of the upper atmosphere. During periods of enhanced geomagnetic activity, such as geomagnetic storms, the upper atmosphere undergoes significant perturbations due to increased energy input from the magnetosphere–ionosphere system. These storms introduce strong variations in Joule heating, particle precipitation, and thermospheric composition, which can modify the propagation conditions of gravity waves and alter tidal amplitudes and phases(Richmond, 1978). In addition, storm-driven changes in background winds and temperature can either enhance or suppress the upward propagation of gravity waves, leading to complex coupling between atmospheric tides and gravity waves (Fritts and Alexander, 2003); (Vadas and Liu, 2009); (Liu et al., 2022). As a result, the response of the upper atmosphere during storm conditions is highly nonlinear and regionally dependent. Recent studies have shown that geomagnetic storms can significantly influence thermospheric temperature, density, and composition, particularly through enhanced nitric oxide (NO) cooling and modified en-

https://doi.org/10.5194/egusphere-2026-4085
Preprint. Discussion started: 4 August 2026

ergy budgets (Fuller-Rowell et al., 1994); (Emmert, 2015). However, while many investigations have focused on either gravity-wave activity or thermospheric energetics independently, fewer studies have examined their simultaneous interaction with atmospheric tides during storm events(Emmert, 2015); (Liu et al., 2022). In particular, the combined role of tidal variability and gravity-wave forcing in modulating storm-time thermospheric responses remains insufficiently understood.

Despite substantial progress in understanding upper-atmospheric dynamics, several key gaps remain. Most previous studies have investigated gravity waves and atmospheric tides separately, without fully addressing their coupled response during geomagnetic storms (Liu et al., 2022); (Yiğit and Medvedev, 2010). The modulation of gravity-wave propagation by tidal background structures during storm-time conditions is still poorly quantified (Oberheide et al., 2011). The relationship between storm-induced energy inputs (e.g., Joule heating and particle precipitation) and the resulting changes in gravity-wave potential energy and tidal variability has not been systematically analyzed using multi-parameter observational datasets (Liu et al., 2022). Furthermore, while NO radiative cooling and heating flux variations have been widely studied in relation to storm-time thermospheric energetics, their connection to tidal modulation and gravity-wave activity remains unclear (Becker and Vadas, 2020). This limits our ability to fully understand how energy is redistributed vertically and horizontally during disturbed space weather conditions. Previous studies have shown that storm-time conditions can amplify tidal components and enhance gravity wave dissipation. However, the detailed interaction between tides and gravity waves during specific storm events remains insufficiently understood, particularly in equatorial and low-latitude regions. This study focuses on the geomagnetic storm of January 19–21, 2026, aiming to: Analyze storm-time variability of migrating atmospheric tides Investigate gravity wave forcing and propagation changes Examine the coupling between tides, gravity waves, and thermal structure

2. Data and Methods

2.1. The Data

The data from solar wind parameters such as solar wind velocity, IMF_Bz, Solar wind plasma flow pressure, eastward electric fields and geomagnetic indices such as the Dst, Kp index, ap index and AU index are downloaded from the data base available `https://omniweb.gsfc.nasa.gov/form/dx4.html` `https://stdb2.isee.nagoya-u.ac.jp/GPS/shinbori/AGRID2/nc/index.`

https://doi.org/10.5194/egusphere-2026-4085
Preprint. Discussion started: 4 August 2026

html. Swarm data obtained from https://swarm-diss.eo.esa.int is used to study ionospheric irregularities, each helped us to monitor ionospheric electron density variations globally. https://data.gats-inc.com/saber/Version2_0/ SABER data level-2A to study atmospheric conditions.

2.2. Methodology

The analysis is based on atmospheric temperature profiles and derived tidal and gravity wave components for three periods: Quiet period before storm: January 16-18, 2026, Storm period: January 19-21, 2026, Quiet period after geomagnetic storm: January 28-30, 2026. Temperature variations in both the lower and upper atmosphere were used to extract tidal and gravity wave signals. Migrating tides were decomposed into their principal components: Diurnal (24 h), Semidiurnal (12 h), Terdiurnal (8 h), Quarterdiurnal (6 h) Amplitude and phase structures were analyzed to identify storm-time modifications. Gravity wave activity was evaluated using: Amplitude variability,Vertical propagation characteristics, and Spatial intermittency Comparisons between quiet and storm periods were used to isolate storm-induced effects. A differential analysis was conducted for Quiet vs storm conditions. This approach enables clear identification of geomagnetic forcing effects.

To quantify tidal variability, the temperature time series T(t,z) was decomposed using Fourier Transform (FFT) into dominant frequency components:

$$T(z,t) = \sum_n A_n(z) cos(\omega_n t + \phi_n(z)) \quad (1)$$

Where A_n= amplitude of the nth tidal component, $\omega_n = \frac{2\pi}{p_n}$ with p_n 24, 12, 8, 6 hours, $\phi_n(z)$= phase , z= altitude FFT Power Spectrum. The discrete Fourier transform (DFT) is applied as $X(f_k) = \sum_{n=0}^{N-1} T(t_e) e^{2\pi i f_k t_n}$ The power spectral density (PSD) is then: $P(f_k) = |X(f_k)|^2$ This allows identification of dominant tidal frequencies: Diurnal, Semidiurnal, Terdiurnal, Quarterdiurnal. To capture non-stationary storm-time variability, we applied the Continuous Wavelet Transform (CWT) using the Morlet wavelet:

$$W(a,b) = \int T(t)\psi^*(\frac{t-b}{a})dt \quad (2)$$

where: a = scale (related to period), b = time localization, ψ = Morlet wavelet The wavelet power spectrum is: P(a,b) =$|W(a,b)|^2$ This method reveals: Temporal evolution of tidal modes and transient enhancements during

https://doi.org/10.5194/egusphere-2026-4085
Preprint. Discussion started: 4 August 2026

storm onset Gravity wave perturbations $T^{'}(z,t)$ were obtained by removing tidal components:

$$T^{'}(z,t) = T(z,t) - \bar{T}(z,t) \quad (3)$$

The gravity wave potential energy per unit mass is:

$$E_p = \frac{g^2}{2N^2}(\frac{T^{'}}{T_o})^2 \quad (4)$$

where: g= gravitational acceleration, N = Brunt-Vaisala frequency, T_o= background temperature

3. Results and Discussion

3.1. Solar Wind and Interplanetary Magnetic Field (IMF) Conditions

The interplanetary evolutionary characteristics of the intense January 19–21, 2026, geomagnetic storm and the resulting solar wind-magnetosphere coupling are displayed in Figure 1. The observations illustrate a highly disturbed interplanetary environment driven by a fast coronal mass ejection (CME) that triggered G4-level (severe) geomagnetic activity. As shown in Figure 1a, the interplanetary magnetic field (IMF) components (Bx, By, Bz) exhibit a sudden, sharp perturbation approximately at 6:00 UT on January 20. At this boundary, the total IMF magnitude intensifies rapidly, and the Bz component turns abruptly southward, plunging to a minimum near -30 nT. This sustained southward Bz orientation satisfies the primary physical condition for enhanced magnetic reconnection at the dayside magnetopause, effectively opening the magnetosphere and facilitating the massive injection of solar wind energy into the Earth's space environment. Concurrently, rapid, high-amplitude fluctuations in the Bx and By components reflect the passage of the highly turbulent magnetic core of the CME structure. Simultaneously, the solar wind plasma velocity (Vsw) panel Figure 1b reveals a prominent shock arrival, with speeds leaping abruptly from a quiet-time baseline of $\sim$ 450 km/s to an extreme peak exceeding 1100 km/s. This massive velocity jump dramatically elevates the kinetic energy flux carried by the solar wind stream. This extreme velocity regime $> 1000km/s$ persists for several hours, ensuring continuous energy input into the inner magnetosphere. The close temporal alignment between the solar wind speed enhancement and the peak southward Bz created optimal conditions for the development of a major geomagnetic storm.

The solar wind dynamic flow pressure plot Figure 1c exhibits a sharp spike exceeding 60 nPa at the storm commencement, representing the sudden

https://doi.org/10.5194/egusphere-2026-4085
Preprint. Discussion started: 4 August 2026

impact of the CME shock compressing Earth's magnetosphere. This high dynamic pressure pushes the magnetopause closer to Earth and dramatically enhances the magnetopause currents. Following this initial shock, the flow pressure decreases but remains significantly elevated, reflecting continued interaction with the dense CME plasma sheath. This sharp pressure pulse is responsible for the sudden commencement (SC) phase of the storm.

The interplanetary electric field (Ey) component Figure 1d intensifies dramatically following the shock. Because Ey is defined as Ey = -(VxB)y = Vsw. Bz in the Geocentric Solar Magnetospheric (GSM) coordinate system, the simultaneous occurrence of extreme solar wind speed and a powerful southward IMF ($Bz < 0$) produces a massive, positive dawn-to-dusk electric field. This strong positive Ey drives intense plasma convection across the magnetosphere and injects high-energy particles into the ring current region.

The response of Earth's ring current is clearly reflected in the Dst index plot Figure 1e. Initially, the Dst index remains near quiet-time levels, but following the arrival of the interplanetary disturbances, it decreases rapidly, reaching a minimum peak of -240 nT. Such a pronounced depression confirms the generation of a severe geomagnetic storm. The minimum Dst occurs several hours after the strongest southward Bz interval, illustrating the characteristic transport and build-up time required for ring current intensification. The global geomagnetic disturbance level is quantified by the Kp and Ap indices Figures 1f and 1g. The Kp index rises dramatically from quiet baseline values < 2 to severe storm levels fluctuating between 7 and 8. These sustained high values indicate widespread auroral expansion and intense high-to-mid-latitude magnetic perturbations. Similarly, the linear ap index increases to values well above 200 nT, confirming the presence of exceptionally strong global magnetospheric ionospheric currents. The presence of multiple peaks in the ap index suggests repeated energy injections driven by the fluctuating interplanetary structures.

Finally, the AE index Figure 1a reaches extreme peaks exceeding 2500 nT, signaling intense auroral electrojet activity and high-latitude substorm processes. The large AE spikes track periods of severe magnetospheric substorms, enhanced particle precipitation, and intense Joule heating in the high-latitude thermosphere. These high-latitude energy dissipation mechanisms fundamentally alter the high-latitude background thermal structure, setting up the physical conditions required to modify thermospheric circulation, distort global atmospheric tides, and launch large-scale acoustic gravity waves.

https://doi.org/10.5194/egusphere-2026-4085
Preprint. Discussion started: 4 August 2026

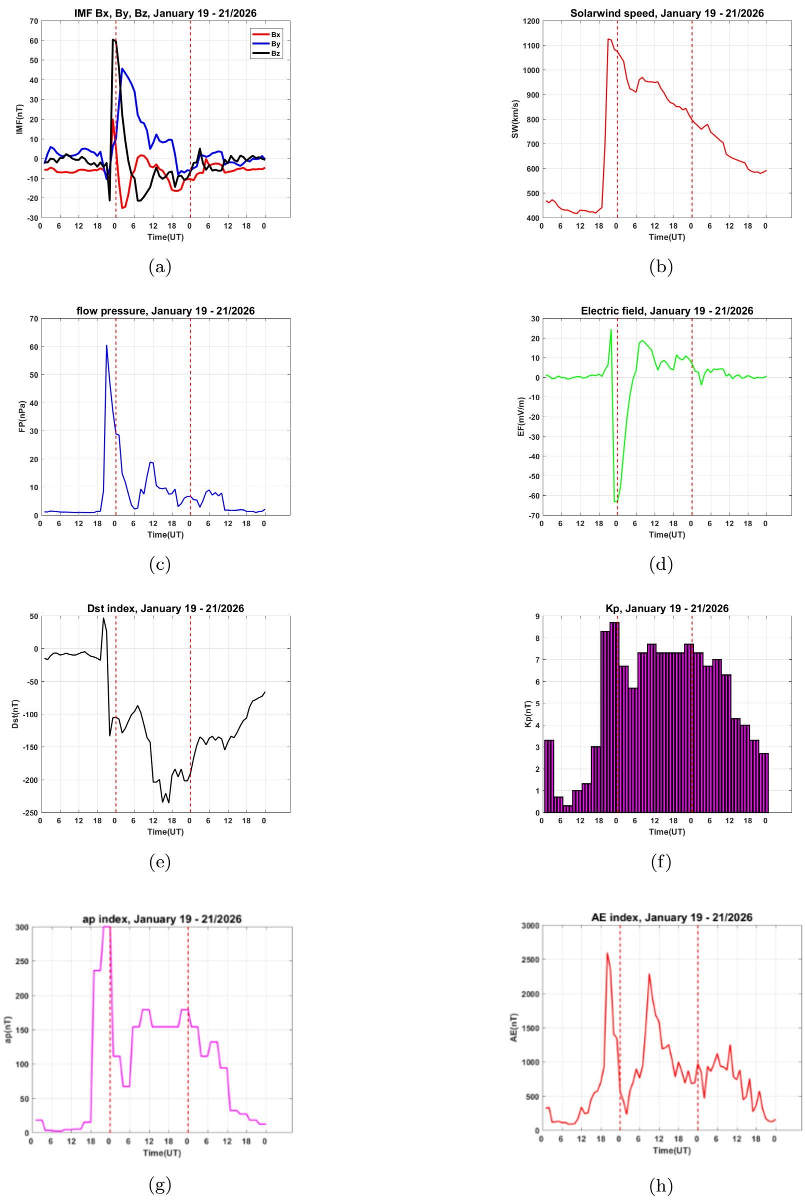

Figure 1: Parameters characterizing the geomagnetic storm of 19–21 January 2026: (a) IMF components, (b) solar wind speed, (c) flow pressure, (d) electric field, (e) Dst index, (f) Kp index, (g) Ap index, and (h) AE index.

https://doi.org/10.5194/egusphere-2026-4085
Preprint. Discussion started: 4 August 2026

3.2. Quiet and storm time Atmospheric Tides

During quiet-time reference periods (January 16–18 and January 28–30), the upper atmospheric tidal structures exhibit a highly stable and coherent behavior. As illustrated in Figure2, the diurnal tidal component dominates

the lower thermosphere, characterized by smooth, linear vertical propagation. Concurrently, the semidiurnal component displays a consistent amplitude profile and steady phase structures, whereas higher-order harmonics specifically the terdiurnal and quarterdiurnal components remain weak. The vertical phase progression across all components is highly regular, indicating minimal external forcing and suggesting that quiet-time tidal variability is primarily governed by periodic solar ultraviolet heating and steady background atmospheric states.

In contrast, during the main phase of the geomagnetic storm (January 19–21, 2026), the migrating tidal structures undergo dramatic modifications. As shown in Figure 3, both the semidiurnal and terdiurnal tides exhibit strong amplitude amplifications, which directly indicate a massive injection of external energy into the mesosphere-lower thermosphere (MLT) and upper thermosphere systems. Concurrently, the vertical phase profiles of these tides become highly irregular and disrupted. This phase distortion suggests a severe modification of the background zonal and meridional wind fields, which alters the refractive index and compromises standard wave propagation pathways.

Furthermore, higher-order harmonic generation becomes structurally prominent during the storm interval, with the quarterdiurnal tide demonstrating a noticeable enhancement in amplitude. This behavior highlights the activation of enhanced nonlinear wave interactions and an accelerated energy cascade across different spatial and temporal scales. The observed storm-time tidal amplifications and structural shifts are primarily attributed to high-latitude auroral processes, including intense Joule heating, localized particle precipitation, and the subsequent re-configuration of global thermospheric wind circulations. These combined high-latitude mechanisms not only provide direct in-situ thermodynamic forcing but also fundamentally alter the underlying wave propagation conditions, allowing lower-atmospheric tides to propagate with modified vertical wavelengths and enhanced amplitudes.

3.3. Gravity Wave Variability

During the geomagnetically quiet intervals of January 16–18 and January 28–30, 2026, atmospheric gravity waves exhibit regular upward propagation, low-to-moderate amplitudes, and highly coherent vertical wave structures.

https://doi.org/10.5194/egusphere-2026-4085
Preprint. Discussion started: 4 August 2026

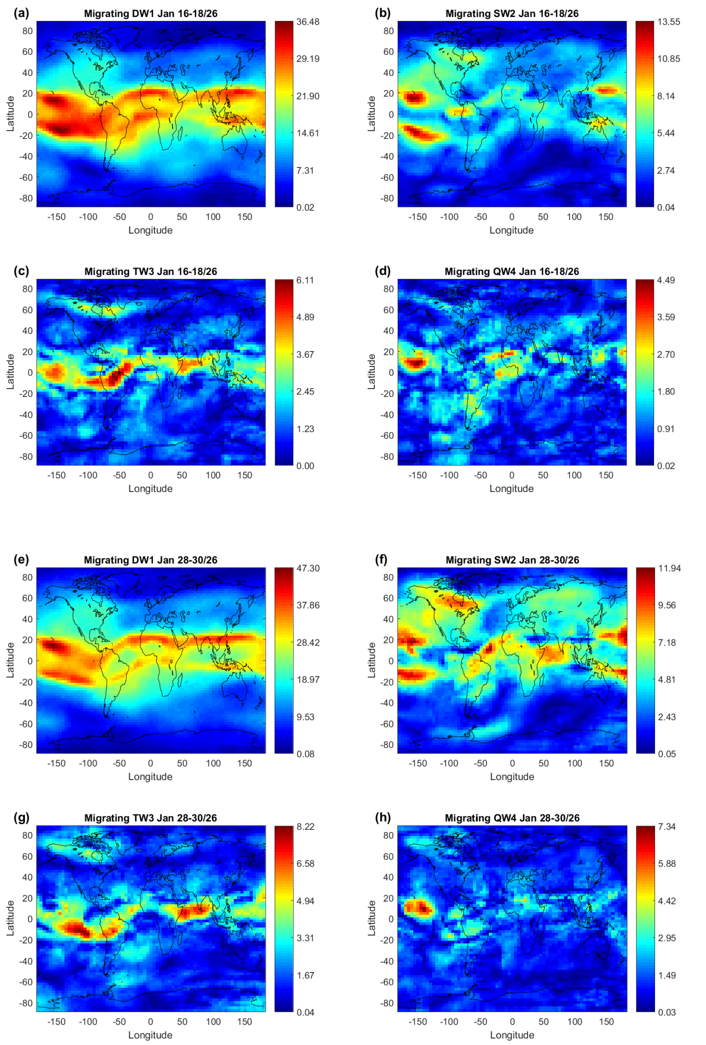

Figure 2: Migrating component of diurnal, semi-diurnal, ter-diurnal and quarter-diurnal waves quiet times from January 16-18/2026 and from January 28-30/2026

https://doi.org/10.5194/egusphere-2026-4085
Preprint. Discussion started: 4 August 2026

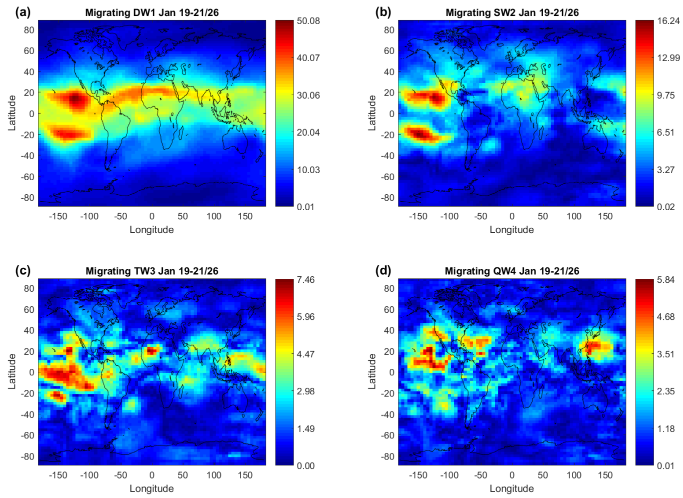

Figure 3: Storm times of migrating tides from January 19-21/2026

As illustrated in the quiet-time panels of Figure 4, these vertical wave packets propagate into the upper atmosphere with minimal structural distortion or background disruption.

Conversely, the storm-time behavior captured during January 19–21, 2026, reveals a starkly altered dynamical regime. Analysis of Figure 4 during the active storm phase demonstrates a significant amplification in wave amplitude, accompanied by strong spatial intermittency and highly irregular structures. Furthermore, vertical penetration into the upper layers is noticeably reduced, indicating enhanced wave attenuation and localized dissipation. Corresponding atmospheric temperature profiles confirm that intense geomagnetic heating within the lower thermosphere markedly steepens vertical temperature gradients and alters local atmospheric stability. These thermal modifications directly modulate both background tidal propagation and gravity wave stability thresholds.

The observed intensification of gravity wave activity during the storm is primarily attributed to a combination of enhanced lower-atmospheric convective sources, secondary wave generation triggered by tidal breaking, and heightened wind shear. This enhanced wind shear induces severe wave filtering. As these gravity waves encounter critical layers and break, they deposit

https://doi.org/10.5194/egusphere-2026-4085
Preprint. Discussion started: 4 August 2026

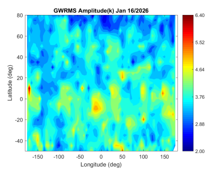

(a)

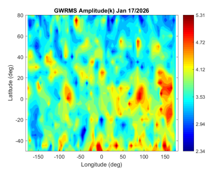

(b)

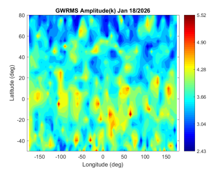

(c)

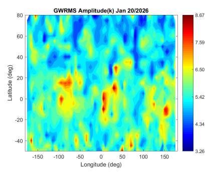

(d)

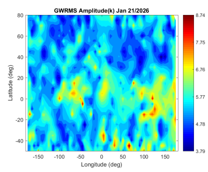

(e)

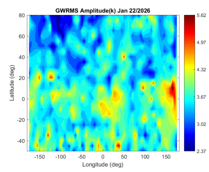

(f)

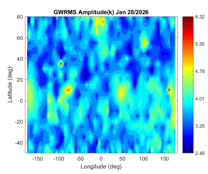

(g)

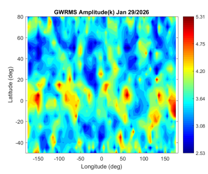

(h)

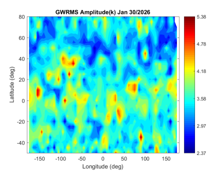

(i)

Figure 4: Gravity wave amplitude of rms temperature perturbation of quiet and storm time January 2026

https://doi.org/10.5194/egusphere-2026-4085
Preprint. Discussion started: 4 August 2026

considerable momentum into the mean flow, subsequently altering the background wind field and heavily modulating the overlying tidal structures.

This bidirectional interaction establishes a highly nonlinear feedback system during the January 19–21, 2026 event. On one hand, upward-propagating gravity waves undergo enhanced dissipation under storm-driven thermal and wind gradients, transferring momentum that significantly modifies the amplitudes and phases of migrating tides specifically the semidiurnal and terdiurnal modes. On the other hand, the large-scale oscillatory tidal winds regulate gravity wave transmission by creating alternating regions of favorable and unfavorable propagation conditions. When a gravity wave's intrinsic phase speed approaches the background tidal wind velocity, it encounters a critical level, leading to localized absorption. Consequently, only a selective subset of the gravity wave spectrum penetrates to higher thermospheric altitudes. This coupled feedback loop is significantly intensified during major geomagnetic storms due to massive high-latitude energy inputs, serving as a primary mechanism for energy and momentum redistribution across the thermosphere-ionosphere system

3.4. FFT Spectral Characteristics of Atmospheric Tides

To quantitatively evaluate the redistribution of atmospheric energy across different temporal scales, Fast Fourier Transform (FFT) analysis was applied to the temperature time series. The resulting frequency spectra reveal fundamental structural transformations between the quiet and disturbed atmospheric states.

During the designated quiet periods Figure 5 a-c and g-i, the temperature diurnal tides display a highly organized, stable, and vertically coherent global structure. Across these baseline days, the tidal amplitudes peak systematically within the MLT region (above 80 km altitude) and near the high southern latitudes (around -50^o), consistently registering maximum variations between approximately 31 K and 42 K. A clear, alternating pattern of warm and cool anomalies can be observed stretching down into the middle atmosphere (30–60 km), showcasing the classic vertical propagation characteristics of migrating diurnal tides under undisturbed background conditions. Even as subtle variations manifest toward the end of the month (Jan 28–30), where a distinct high-latitude northern cooling patch emerges above 100 km, the wave structures retain sharp geographic boundaries and steady phase propagation.

In contrast, the onset of the geomagnetic storm on Figure 5 d-f profoundly disrupts this established global equilibrium. On January 19, the upper-atmospheric response is immediate and violent: the maximum tidal

https://doi.org/10.5194/egusphere-2026-4085
Preprint. Discussion started: 4 August 2026

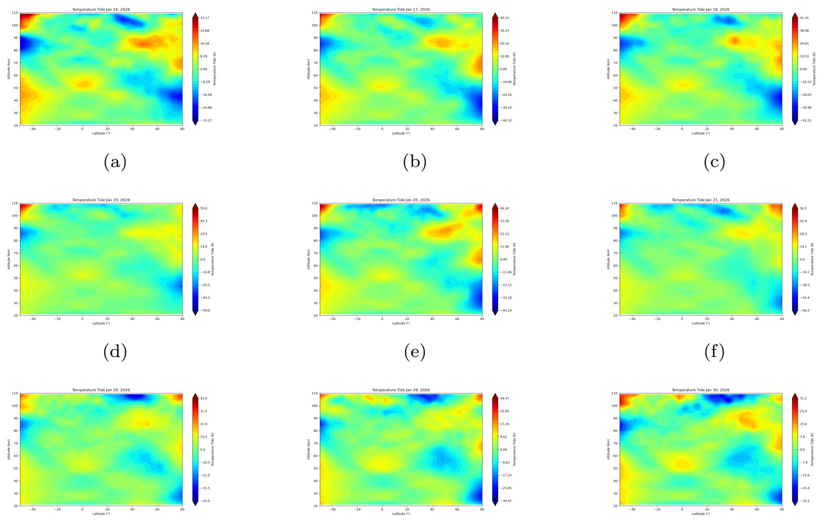

(a) (b) (c)

(d) (e) (f)

(g) (h) (i)

Figure 5: Temperature diurnal tides of quiet and storm time January 2026

amplitude dramatically surges to a peak of 59.0 K, localized predominantly at the highest altitudes and southernmost boundaries. Concurrently, the structured alternating cellular patterns characteristic of the quiet-time profiles are largely washed out or heavily suppressed across mid-and-low latitudes, indicating that energy is being radically redistributed or that the propagating waves are experiencing heavy dissipation.By January 20, the system enters an unstable recovery phase where the absolute maximum intensity contracts back down to around 44.24 K. However, the spatial configuration remains highly distorted compared to the pre-storm baseline. The organized vertical waveforms in the stratosphere and lower mesosphere (20–60 km) appear fragmented and weakened, while the thermospheric structures undergo severe spatial shifting and broadening.

Qualitatively, these changes highlight the intense coupling that occurs between the magnetosphere-ionosphere system and the neutral atmosphere during a space weather event. The massive influx of energy via auroral particle precipitation and Joule heating at high latitudes directly alters the background wind and temperature fields of the upper atmosphere. This sudden modification changes the refractive index of the medium, creating strong filtering zones that block or damp the upward-propagating tidal waves

https://doi.org/10.5194/egusphere-2026-4085
Preprint. Discussion started: 4 August 2026

from below. Simultaneously, the localized auroral heating acts as a powerful in-situ secondary source, driving the temporary, explosive amplification of high-latitude tidal perturbations observed on January 19, before global-scale circulation dynamics act to redistribute and gradually damp the excess energy back toward a quiet-time equilibrium state.

3.5. Thermal Structure Variations During Quiet and Storm Conditions

As presented in Figure 6 a–c illustrates pre-storm quiet-time temperatures, Figure 6 d–f captures storm-time temperatures, and the Figure 6 g–h maps the post-storm quiet-time recovery. A comparative analysis of these panels clearly reveals how the January 2026 geomagnetic storm fundamentally modified the thermal structure of the middle and upper atmosphere.

During the pre-storm quiet period Figure 6a–c, the atmosphere exhibits a relatively smooth, climatological temperature distribution. Temperatures in the lower stratosphere (20–40 km) generally range between 240 K and 280 K, while the mesosphere (70–90 km) encompasses the coldest localized region, featuring temperatures near 180–210 K. Above approximately 95 km, temperatures gradually increase to 260–300 K. During this baseline window, latitudinal temperature gradients remain relatively weak, indicating a stable background atmosphere governed primarily by solar heating, radiative cooling, persistent tides, and nominal gravity wave activity. Furthermore, the mesopause near 85–95 km appears well-defined, which is highly consistent with typical SABER observations where mesopause temperatures commonly range between 160 K and 190 K.

In contrast, the storm-time panels Figure 6, d–f show a pronounced warming that develops above approximately 90–100 km altitude. Relative to the quiet baseline, temperatures increase by roughly 20–50 K, with localized regions exceeding 300 K. The strongest enhancements are concentrated at middle and high latitudes, where geomagnetic energy is directly deposited via auroral particle precipitation and intensive Joule heating. During this January 2026 event, the solar wind speed exceeded 1000km /s and global geomagnetic indices reached severe storm thresholds, facilitating a massive energy transfer from the solar wind into the thermosphere. This rapid energy injection raises neutral temperatures, intensifies global meridional circulation, and launches traveling atmospheric disturbances (TADs) that transport thermal energy away from the auroral zones. Consequently, the temperature contours become considerably more irregular and vertically distorted during the storm phase than during the surrounding quiet intervals. This warming magnitude of roughly 10–20% above the quiet background is

https://doi.org/10.5194/egusphere-2026-4085
Preprint. Discussion started: 4 August 2026

a definitive signature of intense geomagnetic forcing in the lower thermosphere.

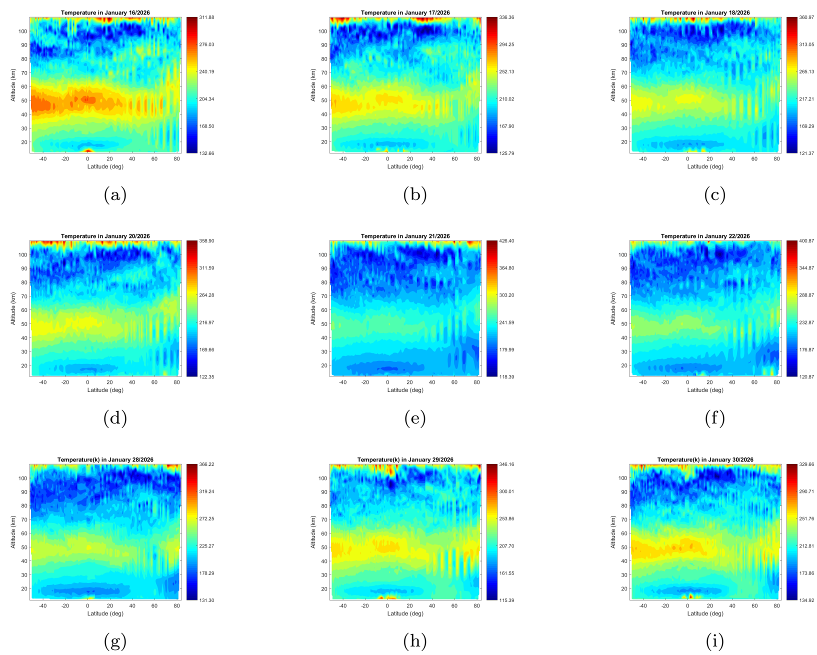

Figure 6: Temperature variation during quiet and storm periods: top panel pre-storm, middle panel during storm and bottom panel post storm periods

Another notable storm-time feature is the structural modification of the mesopause region (80–95 km). The characteristic cold layer becomes visibly less distinct, and mesopause temperatures elevate by approximately 10–20 K compared to the pre-storm baseline. This behavior occurs because storm-driven heating alters the background wind fields, which subsequently changes the propagation, filtering, and dissipation dynamics of atmospheric tides and gravity waves. Enhanced wave breaking deposits substantial momentum and heat into the mesosphere-lower thermosphere (MLT) region, causing a partial erosion of the cold mesopause layer. Such structural variability is typical of storm-time SABER temperature measurements and underscores the tight coupling between thermospheric energetics and middle-atmosphere dynamics.

Figure 6, g–i post-storm quiet-time panels capture the gradual relax-

https://doi.org/10.5194/egusphere-2026-4085
Preprint. Discussion started: 4 August 2026

ation and recovery of the atmosphere as geomagnetic activity subsides. The global temperature profiles regain a smoother latitudinal distribution, and the prominent upper-thermospheric warming seen during the storm peak begins to weaken. Temperatures above 100 km progressively decrease back toward their quiet-time baselines, though some residual warming remains evident. Similarly, the mesopause region begins to re-establish its normal thermal structure, with temperatures returning to the 180–210 K range. However, the upper atmosphere does not recover instantaneously due to the long thermal relaxation time of the thermosphere. Residual circulation changes, altered gravity wave filtering windows, and lingering tidal perturbations can persist for many hours or even several days following the main phase of the storm.

Quantitatively, the most severe storm-related thermal response in Figure 6 occurs between 95 km and 120 km altitude, where absolute temperature enhancements reach approximately 20–50 K relative to the quiet background. In contrast, below about 60 km altitude, temperature changes remain tightly bounded within less than 5–10 K, indicating that the lower atmosphere is insulated from direct geomagnetic energy inputs. Ultimately, these results demonstrate that the January 2026 geomagnetic storm primarily influenced the mesosphere-lower thermosphere region by producing significant upper-atmospheric warming, weakening the cold mesopause layer, amplifying latitudinal variability, and driving enhanced wave activity, while leaving the lower atmosphere comparatively stable.

3.6. Gravity Waves Potential Energy variability (GWPE)

The first row of Figure 7, a–c shows the background gravity-wave environment under relatively undisturbed geomagnetic conditions. GWPE generally increases with altitude, with low values (< 150–$200 Jkg^{-1}$) below about 50 km and stronger values reaching 700-900 J kg^{-1} above 80 km. The enhanced regions are scattered and localized, indicating normal gravity-wave propagation from lower atmospheric sources such as convection, topography, and jet-stream instabilities. The distribution is relatively uniform without large-scale disturbances.

Figure 7,d–f represents geomagnetic storm conditions. Compared with the quiet-time panels, the storm-time maps exhibit a broader spatial distribution of enhanced GWPE in the 80–110 km altitude range. High-energy regions ($> 600 Jkg^{-1}$) appear over larger latitude ranges and occupy a greater fraction of the upper atmosphere. This suggests that the geomagnetic storm has modified the atmospheric circulation and energy balance, resulting in stronger gravity-wave amplification and propagation.

https://doi.org/10.5194/egusphere-2026-4085
Preprint. Discussion started: 4 August 2026

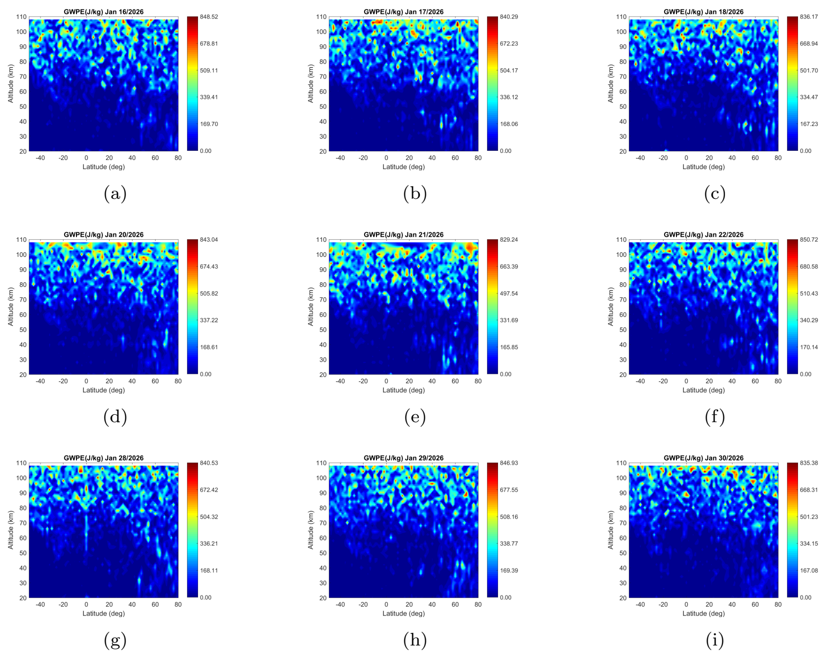

Figure 7: Gravity wave of potential energy of quiet and storm time January 2026

https://doi.org/10.5194/egusphere-2026-4085
Preprint. Discussion started: 4 August 2026

Figure 7, g–i represents quiet conditions after the storm period. The general altitude dependence remains similar, but the GWPE distribution appears less extensive than during the storm-time panels. Although localized maxima still reach 700-900 J kg^{-1}, the regions of enhanced energy are more confined. This suggests that the atmosphere has largely returned to its background state, with gravity-wave activity controlled primarily by meteorological sources rather than geomagnetic forcing.

The storm-time panels exhibit a broader and more persistent enhancement of gravity-wave potential energy in the upper mesosphere and lower thermosphere compared with the quiet-time panels. While peak GWPE values remain comparable ($\sim 900 J kg^{-1}$), the storm-time condition is characterized by a larger spatial extent of high-energy regions above 80 km. This behavior suggests that geomagnetic storm processes enhance gravity-wave activity through thermospheric heating, wind modifications, and secondary wave generation. Following the storm, the GWPE distribution returns toward quiet-time levels, indicating recovery of the background atmospheric state.

One important observation from your figure is that the storm-time GWPE is not dramatically larger than the quiet-time GWPE. This agrees with what you mentioned earlier: in some storms, GW activity can remain similar to or even smaller than quiet-time values because storm-induced wind filtering may prevent some gravity waves from reaching higher altitudes. Therefore, a rigorous conclusion should be based on daily mean GWPE values calculated from the original data, not only on the color maps.

3.7. Radiation cooling

The latitude-altitude distributions of net carbon dioxide and nitric oxide (NO) radiative cooling reveal substantial temporal variations associated with the geomagnetic storm event. During the quiet-time period Figure 8, a–c the cooling rates exhibit a relatively smooth and stable structure, with the strongest cooling concentrated between 100 and 110 km altitude. Peak cooling rates are generally around 2.0-2.5 W m^{-3}, while values decrease gradually with increasing altitude, falling below 0.5 W m^{-3} above approximately 130 km. The strongest cooling occurs predominantly at low and middle latitudes, reflecting the normal thermospheric state in which NO production is controlled primarily by solar EUV radiation and background atmospheric chemistry.

In contrast, the storm-time period Figure 8, d–f shows a pronounced enhancement of NO radiative cooling throughout the thermosphere. Cooling rates increase substantially, with peak values approaching 3.0 W m^{-3} and

https://doi.org/10.5194/egusphere-2026-4085
Preprint. Discussion started: 4 August 2026

enhanced cooling extending to higher altitudes, reaching approximately 125-130 km. The regions of intense cooling become broader and more spatially extensive, particularly over low- and mid-latitude regions. This enhancement is a direct consequence of geomagnetic storm energy input through Joule heating and energetic particle precipitation. These processes increase the production of atomic nitrogen, which subsequently reacts with molecular oxygen to form additional NO. The increased NO abundance leads to stronger infrared emission at $5.3\mu m$, resulting in more efficient radiative cooling of the thermosphere. The widespread enhancement observed during the storm demonstrates the important role of NO as a thermospheric energy-loss mechanism and confirms its function as the "natural thermostat" of the upper atmosphere.

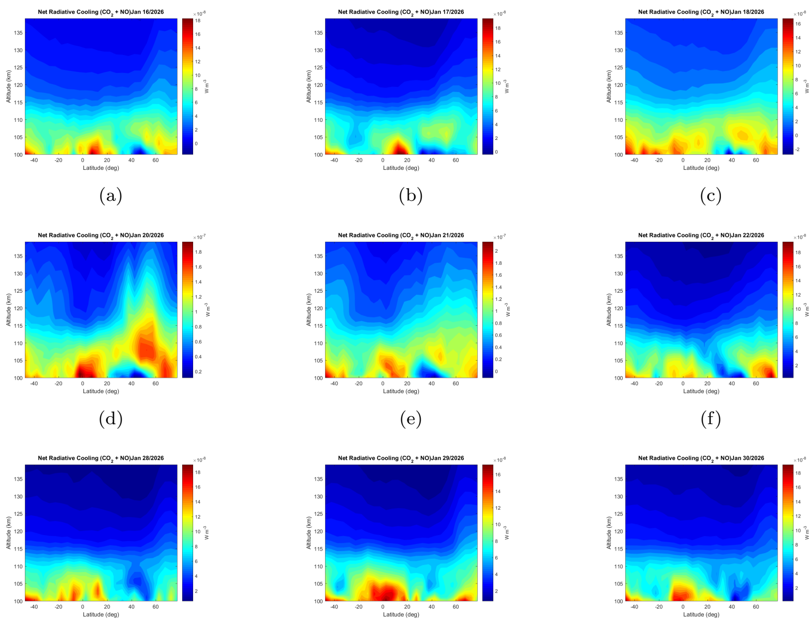

Figure 8: Net radiation cooling(Energy budgeting of atmosphere during quiet , storm time of January 2026

Following the storm, the recovery-phase panels Figure 8, g–i indicate a gradual return toward quiet-time conditions. Although enhanced cooling remains evident, particularly below 115 km altitude, the magnitude and

https://doi.org/10.5194/egusphere-2026-4085
Preprint. Discussion started: 4 August 2026

spatial extent of the cooling decrease compared with the storm peak. Maximum cooling rates generally return to values around 2.0-2.5 W m^{-3}, and the cooling layer becomes more confined to lower altitudes. This behavior reflects the gradual reduction of storm-enhanced NO concentrations through chemical loss processes and atmospheric transport. Nevertheless, residual cooling enhancements persist for some time after the storm, indicating that the thermosphere retains a memory of the storm-induced energy deposition even after geomagnetic activity subsides.

Overall, the results demonstrate that geomagnetic storm conditions significantly increase both the magnitude and vertical extent of NO radiative cooling. Peak cooling rates increase by approximately 20-50% during the storm compared with quiet conditions, while the cooling layer expands upward by roughly 10-20 km. These observations provide clear evidence that storm-time energy deposition strongly modifies thermospheric composition and energetics through enhanced NO production, leading to more efficient radiative cooling and contributing to the restoration of thermal balance in the upper atmosphere.

3.8. Heat flux

The latitude–altitude distributions of atmospheric heating flux during January 2026 show relatively modest variations compared with the NO cooling results, with most heating flux values remaining within approximately 0.4×10^{-3} to $1.4 \times 10^{-3} Wm^2$. During the quiet-time period (top row), the heating flux is generally distributed around 0.6-1.0 $\times 10^{-3} Wm^2$, with only isolated regions exceeding $1.2 \times 10^{-3} Wm^2$. The heating is fairly uniform across latitude and altitude, indicating a thermosphere that is primarily controlled by background solar heating and normal atmospheric dynamics. No extensive regions of intense heating are evident, suggesting that external energy inputs are relatively weak during these undisturbed conditions.

During the storm-time period (middle row), the heating flux exhibits a noticeable enhancement in both magnitude and spatial variability. Larger areas attain values of approximately $1.0 - 1.4 \times 10^{-3} Wm^2$, with localized maxima approaching $1.5 \times 10^{-3} Wm^2$. Compared with the quiet-time conditions, this represents an increase of roughly 20–50% in the strongest heating regions. The enhanced heating is distributed over a wider range of latitudes and extends throughout much of the 100–140 km altitude range. Such increases are consistent with storm-induced energy deposition through Joule heating and particle precipitation, which inject additional energy into the thermosphere and create localized regions of elevated heating flux. The in-

https://doi.org/10.5194/egusphere-2026-4085
Preprint. Discussion started: 4 August 2026

creased spatial variability during the storm also indicates a more disturbed and dynamically active upper atmosphere.

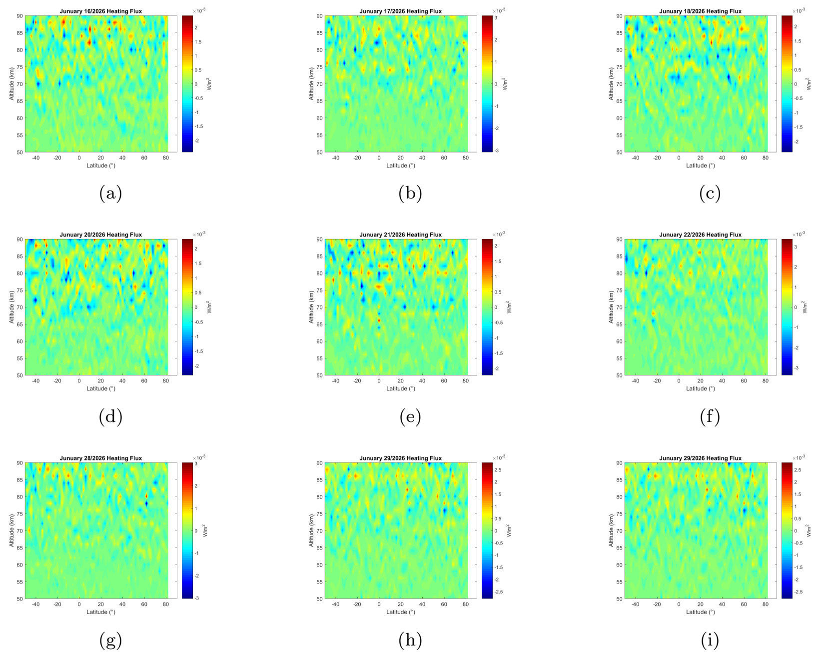

Figure 9: Heat flux of quiet , storm time of January 2026

Following the storm, the recovery-phase panels (bottom row) show a gradual reduction in heating flux. Most values return to approximately 0.6-1.0 $\times 10^{-3} Wm^2$, although some localized regions still exceed $1.2 \times 10^{-3} Wm^2$, indicating that remnants of storm-time energy deposition persist. Compared with the storm peak, both the intensity and spatial coverage of enhanced heating decrease substantially. However, the atmosphere does not immediately return to its initial quiet-time state, reflecting the finite time required for the thermosphere to dissipate excess energy and re-establish equilibrium.

Overall, the results indicate that geomagnetic storm activity enhances atmospheric heating flux from typical quiet-time values of approximately $0.6 - 1.0 \times 10^{-3} Wm^2$ to storm-time values reaching $1.4 - 1.5 \times 10^{-3} Wm^2$. Although the absolute increase appears modest, the relative enhancement of about 20–50% is significant for thermospheric energetics. The storm-time increase in heating flux coincides with the enhanced NO cooling observed in

https://doi.org/10.5194/egusphere-2026-4085
Preprint. Discussion started: 4 August 2026

the previous figure, suggesting that the additional energy deposited during the storm is partially balanced by stronger infrared cooling. This simultaneous increase in heating and cooling demonstrates the thermosphere's response to geomagnetic forcing, whereby excess storm energy is redistributed and eventually removed through radiative processes, helping to restore the thermal balance of the upper atmosphere.

4. Conclusion

This study presents a comprehensive analysis of atmospheric tidal variability and gravity wave forcing during the January 19–21, 2026 geomagnetic storm. The key findings include: Significant amplification of semidiurnal and terdiurnal tides Emergence of higher-order tidal harmonics Enhanced gravity wave activity with strong intermittency Reduced vertical propagation due to increased dissipation Strong coupling between tides, gravity waves, and thermal structure The results demonstrate that geomagnetic storms drive complex multi-scale interactions that significantly modify atmospheric dynamics.

Strong vertical coupling from lower to upper atmosphere Sensitivity of atmospheric dynamics to geomagnetic forcing Importance of multi-scale interactions These findings are critical for improving models of space weather impacts. The present study demonstrates that geomagnetic storms exert a substantial influence on the upper atmosphere by altering its thermal structure, energy balance, and dynamical processes. During storm conditions, enhanced atmospheric heating flux indicates increased energy deposition through Joule heating and particle precipitation, while intensified NO radiative cooling reflects the thermosphere's response to dissipate excess energy and restore thermal equilibrium. Simultaneously, variations in gravity-wave potential energy reveal modifications in atmospheric dynamics and vertical energy transport. The observed increases in heating, cooling, and upper-atmospheric wave activity during storm periods compared with quiet conditions provide clear evidence of strong atmosphere–space weather coupling. Therefore, the results confirm that geomagnetic storms significantly affect the energetics and dynamics of the upper atmosphere, leading to measurable changes in thermospheric composition, temperature, and wave propagation characteristics.

The coordinated responses of GWPE, atmospheric heating flux, and NO radiative cooling demonstrate that geomagnetic storms are capable of significantly perturbing the upper atmosphere, modifying both its energy budget and dynamical behavior. These findings highlight the important role

https://doi.org/10.5194/egusphere-2026-4085
Preprint. Discussion started: 4 August 2026

of geomagnetic forcing in driving upper-atmospheric variability and emphasize the need to consider storm-time effects when investigating thermosphere–ionosphere coupling processes.

5. Acknowledgment

Sincere thanks to reviewers for critical, valuable comments in encouraging the presented unified approach. We gratefully acknowledge the use of data from various sources in this study. The OMNIWeb database provided essential solar wind and interplanetary magnetic field data, accessible through the NASA Goddard Space Flight Center's OMNIWeb platform `https://omniweb.gsfc.nasa.gov/form/dx4.html`. The Global Positioning System (GPS) Total Electron Content (TEC) data were obtained from the International GNSS Service (IGS) via the AGRID-2 project `https://stdb2.isee.nagoya-u.ac.jp/GPS/shinbori/AGRID2/nc/index.html`. `https://data.gats-inc.com/saber/Version2_0/` SABER data level-2A to study atmospheric conditions. Swarm satellite data used in this research were accessed through the European Space Agency (ESA) Swarm Data Access portal `https://swarm-diss.eo.esa.int`. We also acknowledge the use of MATLAB software for processing and analyzing the data, which was instrumental in obtaining the results presented in this paper.

Data Availability Statement

All data used in this study are publicly available at the following URLs:

- `https://omniweb.gsfc.nasa.gov/form/dx4.html`
- `https://stdb2.isee.nagoya-u.ac.jp/GPS/shinbori/AGRID2/nc/index`
- `https://swarm-diss.eo.esa.int`
- `https://data.gats-inc.com/saber/Version2_0/`

Declaration / Data Availability: The authors declare that all data used in this study are publicly available at the above URLs.

https://doi.org/10.5194/egusphere-2026-4085
Preprint. Discussion started: 4 August 2026

References

Becker, E., Vadas, S.L., 2020. Explicit global simulation of gravity waves in the thermosphere. Journal of Geophysical Research: Space Physics 125, e2020JA028034.

Bretherton, F.P., 1969. Momentum transport by gravity waves. Quarterly Journal of the Royal Meteorological Society 95, 213–243.

Chapman, S., Lindzen, R.S., 1969. Atmospheric tides: thermal and gravitational. volume 15. Springer Science & Business Media.

Emmert, J.T., 2015. Thermospheric mass density: A review. Advances in Space Research 56, 773–824.

Forbes, J.M., Maute, A., Zhang, X., 2020. Dynamics and electrodynamics of an ultra-fast kelvin wave (ufkw) packet in the ionosphere-thermosphere (it). Journal of Geophysical Research: Space Physics 125, e2020JA027856.

Fritts, D.C., Alexander, M.J., 2003. Gravity wave dynamics and effects in the middle atmosphere. Reviews of geophysics 41.

Fuller-Rowell, T., Codrescu, M., Moffett, R., Quegan, S., 1994. Response of the thermosphere and ionosphere to geomagnetic storms. Journal of Geophysical Research: Space Physics 99, 3893–3914.

Hagan, M., Forbes, J., 2002. Migrating and nonmigrating diurnal tides in the middle and upper atmosphere excited by tropospheric latent heat release. Journal of Geophysical Research: Atmospheres 107, ACL–6.

Killeen, T., Johnson, R., 1995. Upper atmospheric waves, turbulence, and winds: Importance for mesospheric and thermospheric studies. Reviews of Geophysics 33, 737–743.

Liu, H.L., Lauritzen, P.H., Vitt, F., Goldhaber, S., 2022. Thermospheric and ionospheric effects by gravity waves from the lower atmosphere. Authorea Preprints .

Oberheide, J., Forbes, J., Zhang, X., Bruinsma, S., 2011. Climatology of upward propagating diurnal and semidiurnal tides in the thermosphere. Journal of Geophysical Research: Space Physics 116.

Ortland, D.A., Alexander, M.J., 2006. Gravity wave influence on the global structure of the diurnal tide in the mesosphere and lower thermosphere. Journal of Geophysical Research: Space Physics 111.

https://doi.org/10.5194/egusphere-2026-4085
Preprint. Discussion started: 4 August 2026

Ravinuthala, S., Das, S.K., Nithya, R., Das, S.P., 2022. Ocean, tidal and wave energy: Science and challenges, in: Status and Future Challenges for Non-conventional Energy Sources Volume 1. Springer, pp. 1–21.

Rees, D., 1995. Observations and modelling of ionospheric and thermospheric disturbances during major geomagnetic storms: A review. Journal of Atmospheric and Terrestrial Physics 57, 1433–1457.

Richmond, A., 1978. Gravity wave generation, propagation, and dissipation in the thermosphere. Journal of Geophysical Research: Space Physics 83, 4131–4145.

Vadas, S.L., Liu, H.l., 2009. Generation of large-scale gravity waves and neutral winds in the thermosphere from the dissipation of convectively generated gravity waves. Journal of Geophysical Research: Space Physics 114.

Yiğit, E., Medvedev, A.S., 2010. Internal gravity waves in the thermosphere during low and high solar activity: Simulation study. Journal of Geophysical Research: Space Physics 115.